MATERIALS SCIENCE

Ultrastable piezoelectric biomaterial nanofibers and fabrics as an implantable and conformal electromechanical sensor patch

Tong Li[1,2]†, Yongjiu Yuan[2]†, Long Gu[1], Jun Li[1], Yan Shao[1], Shan Yan[1], Yunhe Zhao[1], Corey Carlos[1], Yutao Dong[1], Hong Qian[3], Xiong Wang[2], Wenlong Wu[2], Steven Wang[2]*, Zuankai Wang[2,4]*, Xudong Wang[1]*

Poly(L-lactic acid) (PLLA) is a widely used U.S. Food and Drug Administration–approved implantable biomaterial that also possesses strong piezoelectricity. However, the intrinsically low stability of its high-energy piezoelectric β phase and random domain orientations associated with current synthesis approaches remain a critical roadblock to practical applications. Here, we report an interfacial anchoring strategy for fabricating core/shell PLLA/glycine (Gly) nanofibers (NFs) by electrospinning, which show a high ratio of piezoelectric β phase and excellent orientation alignment. The self-assembled core/shell structure offers strong intermolecular interactions between the -OH groups on Gly and C=O groups on PLLA, which promotes the crystallization of oriented PLLA polymer chains and stabilizes the β phase structure. As-received core/shell NFs exhibit substantially enhanced piezoelectric performance and excellent stability. An all NF–based nonwoven fabric is fabricated and assembled as a flexible nanogenerator. The device offers excellent conformality to heavily wrinkled surfaces and thus can precisely detect complex physiological motions often found from biological organs.

INTRODUCTION

Piezoelectricity is a common physical phenomenon that couples mechanical strain with electricity (*1*–*3*). This property enables many important applications for biomechanical devices where electromechanical coupling is often observed, such as biosensors, ultrasonic transducers, and electrostimulation devices (*4*–*10*). These devices usually need to be directly integrated with the soft tissues and organs in biological systems. This requires biocompatibility and biodegradability, especially flexibility that can match tissue mechanically to reduce the risk of tissue injury and decrease burdens on organ functions (*11*–*13*). Unfortunately, the popular and frequently used piezoelectric materials represented by inorganic lead zirconate titanate and polymeric polyvinylidene fluoride can only meet part, but not all, of these properties and thus cannot be the ideal solution for clinical trials (*14*–*17*). Poly(L-lactic acid) (PLLA), a biocompatible and biodegradable medical polymer used extensively in U.S. Food and Drug Administration–approved implants, has been found to be piezoelectric owing to their electrical polarity of the carbon-oxygen double bonds (C=O) branching out from its backbone (*18*–*21*). It offers a promising potential platform to develop safe, biodegradable piezoelectric implants. However, its weak and unstable piezoelectricity still stands as a big challenge for achieving practical applications. The ultimate solution to this limitation is to maximize the piezoelectric phase and perfectly align the polarization orientation. Although the crystallinity and alignment can be improved by thermal annealing and mechanical stretching, stretched piezoelectric PLLA bulk films usually have a low β phase ratio, poor stability, and high rigidity (*22*–*24*).

Recognizing these critical challenges, electrospinning is effective in producing self-poled soft piezoelectric PLLA nanofibers (NFs) with high crystallinity because of the high stretching forces exerted on electrified solution jets (*12*, *25*, *26*). Nevertheless, the polarized PLLA will be partially rearranged under mechanical stretching or even temperature fluctuation via thermal motion, thus tending to be depoled or relaxed back to the more thermodynamically stable nonpiezoelectric phases. Here, we presented a one-step strategy to address the long-standing stability issue in piezoelectric PLLA NFs by introducing glycine (Gly) as a heterogeneous nucleating agent. Self-assembly of Gly into a shell layer was essential for the formation and alignment of β phase PLLA, where the strong intermolecular interaction at the interface between Gly and PLLA was responsible for anchoring the self-poled PLLA chains and promoting crystalline nucleation. As-received core/shell NFs exhibited substantially enhanced piezoelectric performance and excellent stability. As a result, the core/shell NFs could act as an effective flexible piezoelectric sensing element. In vivo application of the core/shell NFs was demonstrated as an implantable device to recognize the intestinal peristalsis at different states with excellent stability and biocompatibility. This work presented a practical strategy to address the long-standing stability issue in piezoelectric PLLA nanostructure fabrication and opened a door to the development of flexible and biodegradable electromechanical coupling devices for biomedical applications.

RESULTS

To address the orientation and instability issues of piezoelectric PLLA, we propose that introducing Gly to PLLA electrospun solution can provide heterogeneous nucleating sites to stabilize the oriented PLLA C=O dipoles (Fig. 1A). During the electrospinning process, a direct current (DC) electric field of 1.5 kV/cm was applied

---

[1]Department of Materials Science and Engineering, University of Wisconsin-Madison, Madison, WI 53706, USA. [2]Department of Mechanical Engineering, City University of Hong Kong, Hong Kong 999077, China. [3]Department of Orthopedic, Nanjing Jinling Hospital, Nanjing 210002, China. [4]Department of Mechanical Engineering, The Hong Kong Polytechnic University, Hong Kong 999077, China.
*Corresponding author. Email: steven.wang@cityu.edu.hk (S.W.); zk.wang@polyu.edu.hk (Z.W.); xudong.wang@wisc.edu (X.W.)
†These authors contributed equally to this work.

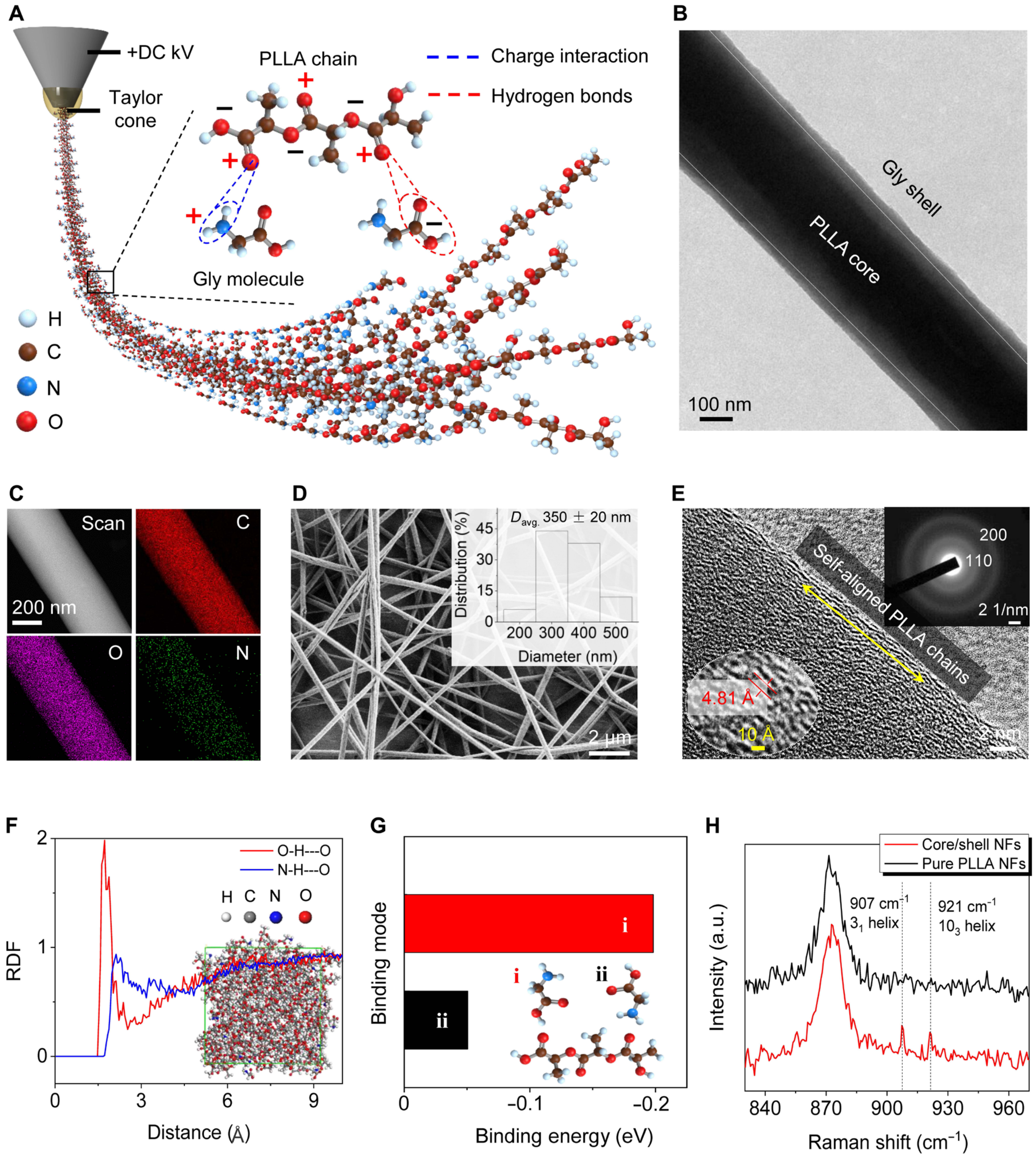

Fig. 1. Formation mechanism of core/shell PLLA/Gly NFs. (**A**) Schematic of the PLLA chain arrangement and orientation induced by intermolecular interactions during the electrospinning process for the fabrication of core/shell PLLA/Gly NFs. (**B**) TEM image showing the core/shell structure of PLLA/Gly NF. (**C**) Energy dispersive spectroscopy mapping of C (red), O (purple), and N (green) elements distribution in a PLLA/Gly core/shell NF shown in the TEM image (upper left). (**D**) SEM image of core/shell NFs showing their uniform sizes with average diameters ($D_{avg.}$) of 350 ± 20 nm. (**E**) HRTEM, the enlarged view of HRTEM (lower-left inset), and SAED images (upper-right inset) of a core/shell NF showing aligned PLLA chains along the fiber axis. (**F**) RDFs between the C=O groups in PLLA and the -OH (red) and $-NH_2$ (blue) groups in Gly. The inset is the MD simulations of a PLLA/Gly molecular structure in equilibrium, showing the core (PLLA)/shell (Gly) arrangement. (**G**) DFT-calculated binding energies for the two binding situations. Inset: schematics of two possible ways for Gly molecules to bind with PLLA chains. (**H**) Raman spectra of the core/shell (red) and pure PLLA (black) NFs in the range of 830 to 970 cm^{-1}. a.u., arbitrary units.

between the needle and the collecting plate. Under this high positive electric field, the positively charged $-NH_2$ groups in Gly molecules would be repelled from the inside to the surface of the molten fiber. Meanwhile, the -OH groups on Gly preferentially interacted with the C=O groups on the PLLA chain via hydrogen bonds, forming a stable C=O---HO dipole array at the interface (Fig. 1A, inset). This intermolecular anchoring effect along the Gly-PLLA interface would direct the nucleation of β-PLLA with ordered C=O orientation chains (i.e., 3_1 helical conformation). As a result, PLLA/Gly core/shell NFs were obtained with uniform diameters of ~350 ± 20 nm, where a continuous Gly shell (thickness of 20 ± 5 nm) tightly wrapped around the entire PLLA NF core (Fig. 1, B to D, and fig. S1). High-resolution transmission electron microscopy (HRTEM) confirmed the self-oriented PLLA crystalline chains (Fig. 1E and fig. S2). It could be seen that most of the PLLA chains were aligned and oriented parallel to the PLLA/Gly interface. The interchain distance was 0.48 ± 0.01 nm (Fig. 1E, lower-left inset), corresponding to the (200) plane of β phase PLLA, which was also revealed by the selected-area electron diffraction (SAED) pattern (Fig. 1E, upper-right inset). As a comparison, pure PLLA NF without Gly showed a lower content of the β phase with a disordered arrangement (fig. S3). This further confirmed the critical role of interfacial C=O---HO bonding in promoting the formation and alignment of β-PLLA.

The molecular interactions between Gly and PLLA were further confirmed by molecular dynamic (MD) simulations (Fig. 1F and fig. S4A). Comparing the radial distribution functions (RDFs) of O atoms on PLLA chains next to the $-NH_2$ groups (N–H---O) and next to the -OH groups (O–H---O), O–H---O RDF showed an obviously higher value of 2 to 3 Å, confirming that the C=O bonds on PLLA would preferably bond to the -OH groups on Gly. This could guide and anchor the orientation of C=O groups on PLLA chains and thus held the β phase and its macroscopic orientation stably. Density functional theory (DFT) was used to further confirm the interactions between Gly and PLLA. When a Gly molecule had its -OH groups bound with the C=O groups on PLLA chains, the overall system energy reached the minimum (Fig. 1G and fig. S4B). Without Gly to balance the dipole in PLLA, 10_3 helical conformations in pure PLLA NFs would dominate and minimize the internal electrostatic energy. Parallel to theoretical simulations, Raman spectroscopy was used to characterize molecular interactions between Gly molecules and PLLA chains (Fig. 1H). The C-COO stretching vibration at 872 cm^{-1} was strengthened by the electrostatic attractions between the -OH groups in Gly and the C=O groups on PLLA. The peaks at 907 and 921 cm^{-1} assigned to the coupling of the CH_3 wagging vibration and C-C stretching vibration were substantially enhanced as well, with the former reflecting to the 3_1 helix (β crystals) and the latter to the 10_3 helix (α crystals). This was a result of the strong interactions between the -OH groups on Gly and the C=O groups on PLLA as further reflected by x-ray photoelectron spectroscopy (fig. S5). All the strengthened peaks in Raman spectra suggested an increase in crystallinity of the core/shell NFs. Particularly, the strengthened peaks at 872 and 907 cm^{-1} indicated a high percentage of oriented β phase PLLA with the chain orientation along the fiber axial direction, matching well to HRTEM results.

To further understand the role of the Gly shell in the formation of β-PLLA, NFs were fabricated via the same approach at various Gly-to-PLLA ratios from 0 to 1:80. One-dimensional (1D) and 2D x-ray diffraction (2D XRD) were first used to evaluate the crystallinity and the molecular chain orientation of the PLLA/Gly NFs. As shown by the 2D XRD in Fig. 2A, NFs with core/shell structure obtained at a Gly-to-PLLA ratio of 1:120 exhibited the strongest (200) diffraction peak corresponding to the β phase PLLA, whereas a diffraction ring pattern was obtained from the pure PLLA NFs, suggesting randomly oriented polymer chains. This difference could be illustrated by the azimuthal-integrated intensity distribution curves derived from the 2D XRD spectra (fig. S6). The orientation parameter was calculated from the azimuthal-integrated intensity distribution curves to quantify the degree of orientation of the polymer chains in NFs (detailed calculation process is included in text S4), where the core/shell NFs yielded the highest value of 0.88 (Fig. 2B). This suggested that most of the PLLA chains were aligned along the same direction in the core/shell NFs. 1D XRD spectra (Fig. 2C) further showed that NFs with a Gly-to-PLLA ratio of 1:120 had a dominating β phase, while all other PLLA/Gly NFs exhibited a coexistence of both α and β phases. The crystalline ratio of β-PLLA was quantified by analyzing differential scanning calorimetry (DSC) thermogram and Fourier transform infrared (FTIR) spectroscopy. The crystalline ratios (Xc) of PLLA/Gly NFs were determined from DSC peak intensity (fig. S7A and text S5). The FTIR spectra showed the characteristic β phase peak at 872 cm^{-1} and characteristic α phase peak at 923 cm^{-1} from all samples (fig. S7B), from which the β phase ratios [F(β)] were derived (detailed calculation process is included in text S6). The β phase crystallinity was then calculated by Xc × F(β) × 100%. All F(β), Xc, and β phase crystallinity showed the same trend following the Gly concentration (fig. S7C), where the β crystallinity reached the highest value of 64% at a Gly-to-PLLA ratio of 1:120 (Fig. 2B). Low Gly content (Gly-to-PLLA ratio of 1:240) yielded low crystallinity and poor spatial orientation. This was because an insufficient amount of Gly could not form a continuous shell to completely confine the PLLA core (fig. S8). On the contrary, overloaded Gly may exceed the phase separation threshold and the core/shell structure vanished (fig. S9). Mixing Gly in the PLLA matrix would disrupt the orientation and alignment of PLLA chains and thus led to lower crystallinity. Therefore, continuous and uniform anchoring effect at the core/shell interface is essential for the formation of β-PLLA and alignment of its molecular chain orientation.

The high β phase content and well-aligned dipole orientation in the core/shell NFs are expected to largely enhance their piezoelectricity. The piezoelectric property was first characterized from individual NFs by piezoresponse force microscopy (PFM). By applying an electric bias between the PFM tip and conductive substrate ranging from 1 to 5 V (fig. S10), all NF samples showed a voltage-dependent increase in displacement, where the core/shell NFs exhibited obviously higher amplitudes compared to other NFs. The effective piezoelectric coefficients along the diameter direction ($d^{\mathrm{eff}}{}_{33}$) were derived from the slopes of the displacement versus applied voltage curves. The core/shell NFs exhibited the highest $d^{\mathrm{eff}}{}_{33}$ value of 2.21 pm V^{-1}, which was 2.5 times of that of pure PLLA NFs (Fig. 2D). This piezoelectricity enhancement is directly correlated with the crystallinity and orientation improvements as a result of the Gly shell. The bulk-scale piezoelectricity of the NFs was further tested from a nonwoven fabric (20 × 10 mm^2 in size and 50 μm in thickness) made by randomly spraying the NFs and then coated with top and bottom electrodes. When the fabric (made from the NFs with a Gly-to-PLLA ratio of 1:120) was repeatedly pressed at a frequency of ~4 Hz over a vertical distance of 8 mm, a stable voltage output with a peak-to-peak voltage (V_{pp}) of 1.2 V was obtained (fig. S11). Fabrics assembled from PLLA/Gly NFs at other Gly concentrations also generated piezoelectric outputs under the same deflection but with much lower amplitudes (Fig. 2D and fig. S12). This result is consistent with the individual NF measurements.

The PLLA/Gly core/shell structure successfully addressed the long-term stability issue of piezoelectric PLLA, which was usually at the level of several days due to the depolarization of PLLA crystals (*12*, *27*). As expected, pure PLLA NFs dropped from 0.32 to 0.23 V on day 7 and completely lost its piezoelectricity in day 14 (Fig. 2E, black, and fig. S13). Notably, fabrics made from our core/shell NFs

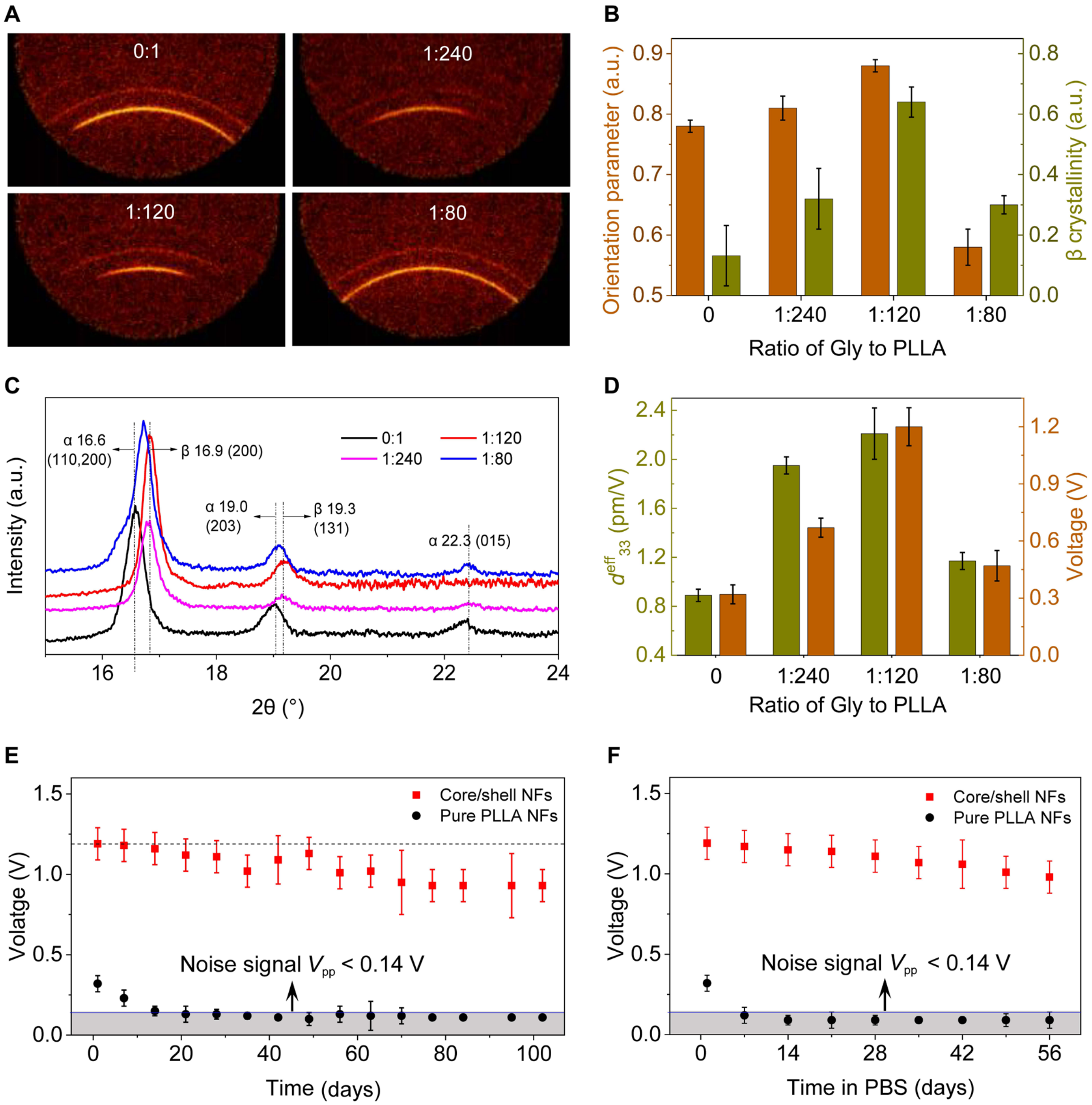

Fig. 2. Crystallinity characteristics and piezoelectric property of PLLA/Gly NFs. (**A**) 2D XRD images of PLLA/Gly NFs with different Gly contents. (**B**) Orientation parameter and the crystallinity percentage as a function of the Gly content, quantified from 2D XRD and the 1D XRD spectra, respectively. (**C**) 1D XRD spectra of PLLA/Gly NFs with different Gly contents. (**D**) Measured d^{eff}_{33} coefficients and piezoelectric voltage of PLLA/Gly NFs with different Gly contents. (**E**) Comparison of output voltages of pure PLLA NFs and core/shell PLLA/Gly NFs after 102 days of storage in a conventional environment. (**F**) Comparison of the output voltage before and after the pure PLLA NFs and core/shell PLLA/Gly NFs being immersed in a PBS solution for 56 days. $n = 8$ independent piezoelectric stability experiments in dry and liquid environments showing similar results. All error bars indicate ± SD.

(Gly-to-PLLA ratio of 1:120) could retain ~78% of their initial piezoelectric output and remain stable even after 102 days (Fig. 2E, red, and fig. S13). Such a high stability can be attributed to the continuous and uniform anchoring effect at the core/shell interface (fig. S14). To further show the stability in a liquid environment that can be commonly interact in a biological system, the fabrics were immersed in a phosphate-buffered saline (PBS) solution at room temperature, and their piezoelectric outputs were evaluated once a week (Fig. 2F and fig. S15). The PLLA/Gly core/shell NF fabric showed a nearly unchanged V_{pp} during the first 7 days and only dropped by ~20% on day 56. On the contrary, the V_{pp} of pure PLLA NF fabric completely lost its piezoelectricity within 7 days. The substantially enhanced water stability of the PLLA/Gly core/shell NF could be attributed to the high crystallinity of the PLLA phase (fig. S16), which could slow down the infiltration and interaction of water molecules to dissociate PLLA chains (*28*). Scanning electron microscopy (SEM) and optical images revealed that many pure PLLA NFs started to collapse after 7 days in liquid, while the core/shell NFs were nearly intact throughout the 56-day testing period (fig. S17). The core/shell PLLA/Gly NFs can degrade completely in PBS solution, which could be visualized after a 49-day period in an accelerated degradation process at 70°C (fig. S18). In addition to the stable and long shelf-life, the β-PLLA/Gly core/shell NF films could also retain a stable piezoelectric output during continuous strain actions for more than 30,000 cycles (fig. S19).

The NF morphology and their random assembly offer excellent flexibility to the fabric structure, allowing it to achieve conformal attachment to heavily wrinkled surfaces, which are commonly seen in biological systems such as the brain, colon, etc. This capability was first demonstrated using a crumpled elastic latex tube to simulate the heavily wrinkled tissue surfaces (fig. S20A). The NF fabric was able to remain a seamless attachment to the crumpled surface when it was either relaxed or stretched (fig. S20B and movie S1). Subsequently, the piezoelectric performance was evaluated on the wrinkled surfaces under large displacements. A flexible piezoelectric nanogenerator (NG) was made using an NF fabric packaged by polydimethylsiloxane (PDMS) (10 × 15 mm^2 and 50 μm in thickness) with a pair of gold electrode layers (fig. S21A). The NG was directly attached to the crumpled elastic tube surface (Fig. 3A and fig. S21B). The crumbled tube was inflated repeatedly at a frequency of ~1 Hz to introduce periodic expansion and retraction motions to the fabric NG. This motion stretched the fabric and generated the electric potential difference on the two electrodes (Fig. 3A, bottom). Periodic voltage output with a V_{pp} of ~0.8 V was recorded following

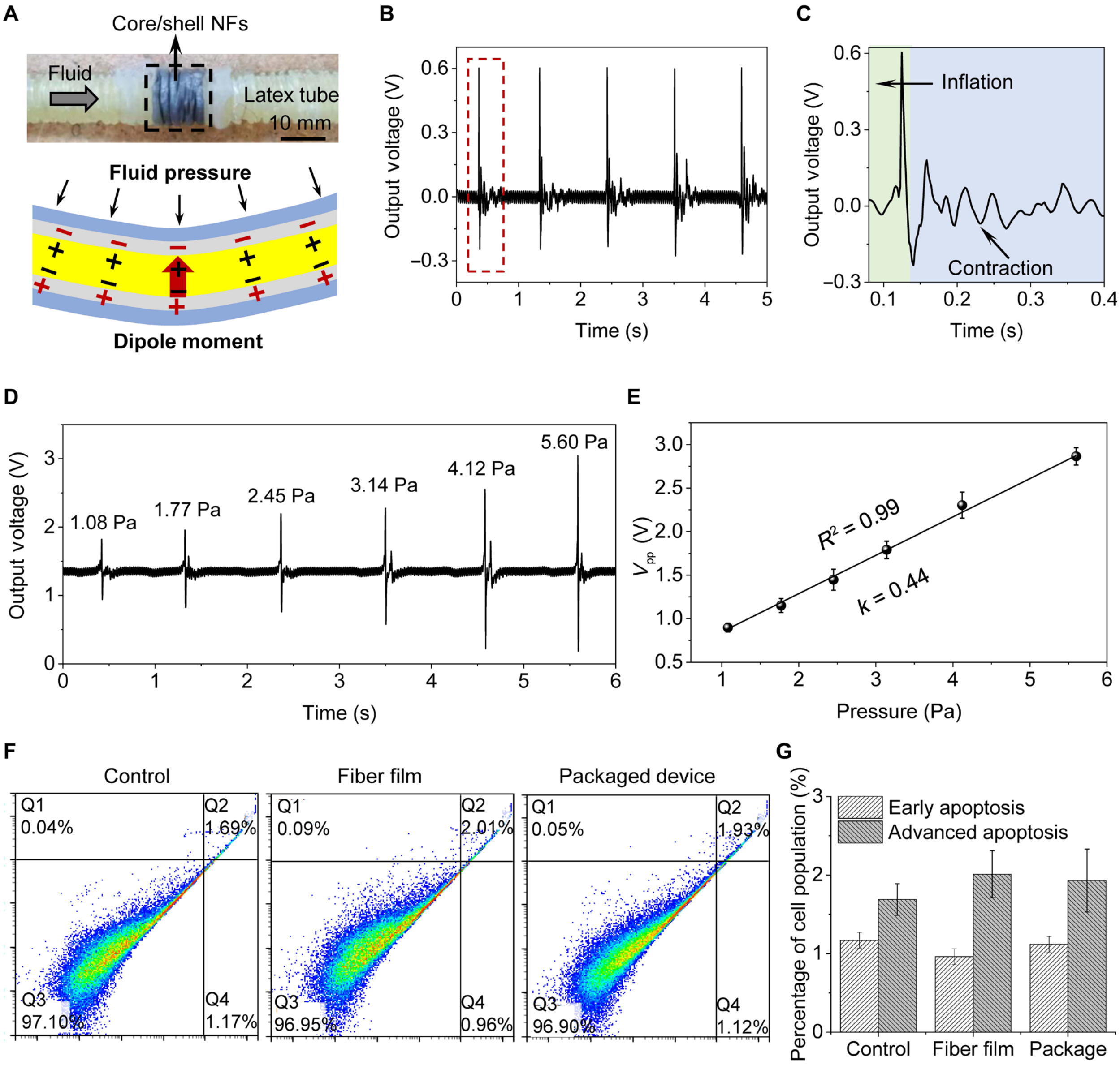

Fig. 3. Flexibility and cytocompatibility of core/shell NFs. (**A**) PDMS-packaged core/shell fibrous film showing excellent flexibility, matching well with the wrinkled elastic tube (top). The charge distributions are in response to fluid pressure. (**B**) Output voltage response in the process of tube inflation and contraction. (**C**) Detailed voltage signals from the enlarged area of the red dashed box in (B). (**D**) Voltage response as a function of injection water. (**E**) Linear fitting of V_{pp} and pressure change. (**F**) Apoptosis images of PC12 cells after 3 days cultured on a cell culture dish, core/shell NFs, and packaged device. (**G**) Percentage of early and advanced apoptotic cells. All error bars indicate ± SD. $n = 3$ independent cell experiments showing similar results.

the inflation motions (Fig. 3B). A zoomed-in single peak is shown in Fig. 3C, where the peristaltic relaxation of the tube (water injection) yielded the positive voltage signal, and the negative voltage was induced by its peristaltic contraction (water reflux). Owing to the piezoelectricity nature, the V_{pp} output of the NG scaled from 0.9 to 2.9 V as the internal pressure increased from 1.08 to 5.60 Pa (Fig. 3D). This voltage-pressure relationship exhibited an excellent linearity with $R^2 = 0.99$ (Fig. 3E). The slope of the curve was determined to be 0.44 V/Pa within the measured pressure range, suggesting that this conformal NF film may serve well as a pressure sensor.

Before in vivo implantation experiments, the biocompatibility of core/shell NFs was first tested in vitro by cell apoptosis assay. PC12 cells were cultured on the core/shell NF films without and with PDMS package for 3 days. The cell apoptosis was then evaluated by flow cytometry. In the apoptosis diagram, Q1, Q2, Q3, and Q4 represented mechanical injury dead cells, nonviable apoptotic cells, normal cells, and early apoptotic cells, respectively (Fig. 3, F and G). It was found that the cell viability (Q1 value) from both the NF film samples was greater than 96%, with no substantial difference compared to the control group. Besides, the Q4 values of cells on NF films without (0.96%) and with (1.12%) packages were both lower than that of the control group (1.17%), while their Q2 values were not substantially different, suggesting that the NF film and its package did not affect the cell cycle. These data confirmed that the PLLA/Gly NFs were biocompatible and nontoxic and can be used for implantable biomedical devices.

To demonstrate the in vivo application potential on heavily wrinkled tissue surfaces, the PDMS-packaged NF-based NG was implanted onto the intestinal wall of transverse colon, which showed a complex wrinkled structure (Fig. 4A). Soft silver-plated polytetrafluoroethylene (PTFE) Teflon wires serve as conductors to transmit electrical signals to prevent rigid modules from affecting the response to weak mechanical stimulation (fig. S22). This implant site was the longest and most mobile part of the colon and played an essential role in digestion and the excretion of waste products. The NG was attached to the external surface of colon walls using bioglue. It exhibited an excellent conformality to the colon surface without showing any detachments (Fig. 4A, right). The highly compatible and conformal attachment of the PLLA/Gly NF film allows it to move and deform following the colon wall's motions and convert the mechanical force into electric signals (Fig. 4B). Collecting the motion patterns there (frequency and amplitude) allows identification of the peristalsis states and assessing the health status of the gastrointestinal tract. To initially assess this capability, we administered enemas to rats using a urinary catheter at a frequency of ~0.2 Hz. It was clear that the NF film yielded a stable V_{pp} of >2 V in response to each peristalsis (fig. S23). Notably, each voltage output from one colon peristalsis action comprised multiple voltage peaks forming an envelope of signal output. This was because the heavily wrinkled surface underwent multiple localized expansions/contractions as peristalsis occurred in the intestine. The signal output envelops evidenced that the conformal NGs were able to recover the complete motion of the colon, providing an effective approach to colon monitoring. This function may be useful for diagnosis of gastrointestinal diseases, such as intestinal obstruction, Ogilvie's syndrome, and acute colitis.

To show the diagnosis capability, we proposed the onset and remission of acute colitis as a representative disease (Fig. 4C). Ten days before induction of colitis, rats underwent NG implantation that tightly adhered to the intestinal wall of transverse colon. Subsequently, acute colitis was induced by feeding rats with dextran sulfate sodium (DSS) in their drinking water for 7 days. Last, the rats underwent colitis relief by drinking 3-day normal water. The occurrence and recovery of acute colitis could be observed directly from hematoxylin and eosin (H&E) staining (Fig. 4D). Meanwhile, this process was reflected in real time and accurately by the recorded voltage signals (Fig. 4E and fig. S24). It was shown that rats with colitis display an overall increased propulsive (of both high- and low-amplitude voltage) activity compared with normal rats and similar to that found in patients with diarrhea-predominant irritable bowel syndrome (*29*). No differences were found between rats in remission of colitis and normal rats in terms of high-amplitude propulsion (high-amplitude voltage), while low-amplitude propulsion activity (low-amplitude voltage) increased substantially (Fig. 4F and figs. S25 and S26). The signals from rat colitis by removing the DSS aqueous solution was accurately recorded in real time. This revealed the process of colitis recovery when treated with drugs, thereby demonstrating the ability of assisting disease treatments. These measurements confirmed that our PLLA/Gly NF-based NGs were able to precisely detect the motion patterns in colonic peristalsis including amplitude and frequency, providing critical information for early diagnosis and medical prevention/intervention of gastrointestinal diseases, which can even be used to evaluate the efficacy of some previously unidentified gastrointestinal drugs.

Long-term in vivo biocompatibility of the device is also an important parameter, and inflammation analyses were performed by staining prepared tissue slides from the colon and muscle around the implant site. The implants were taken out after 1 and 5 weeks of implantation. The histological images of the implantation area during the first week showed a very mild immune reaction without notable presence of inflammation and cellular toxicity (Fig. 4G, left panel). In the fifth week, they completely returned to normal levels. These data showed that the PLLA/Gly NF-based NGs had good biocompatibility and could maintain stable performance over a long time in biological environment. Pathological tests were also conducted on vital organs, including heart, liver, spleen, lung, and kidney. H&E staining was collected from these organs at different time points (days 1 and 35) after implantation. All the organs showed no deformation or abnormal lymphatic cell invasion (Fig. 4G, right panel), which further confirmed that all rats were in good health condition and the device had no systemic side effects.

DISCUSSION

In summary, we developed a one-step electrospinning approach to the fabrication of core/shell PLLA/Gly NFs. The self-assembled core/shell structure was attributed to the formation of a continuous Gly shell upon solidification as a result of electrostatic repulsion to Gly molecules. This core/shell structure was found essential for the formation of the piezoelectric phase and alignment of PLLA polymer chains, where strong intermolecular interaction between the -OH groups on Gly and C=O groups on PLLA was responsible for aligning the PLLA chains and promoting β phase nucleation. A high β phase ratio of 64% was identified from the PLLA/Gly NFs. This continuous interfacial anchoring effect was also able to improve the β phase stability. As a result, the piezoelectricity from the β phase PLLA in the as-received core/shell NF could remain stable over 100 days, while pure PLLA NFs completely lost its piezoelectricity in 14 days.

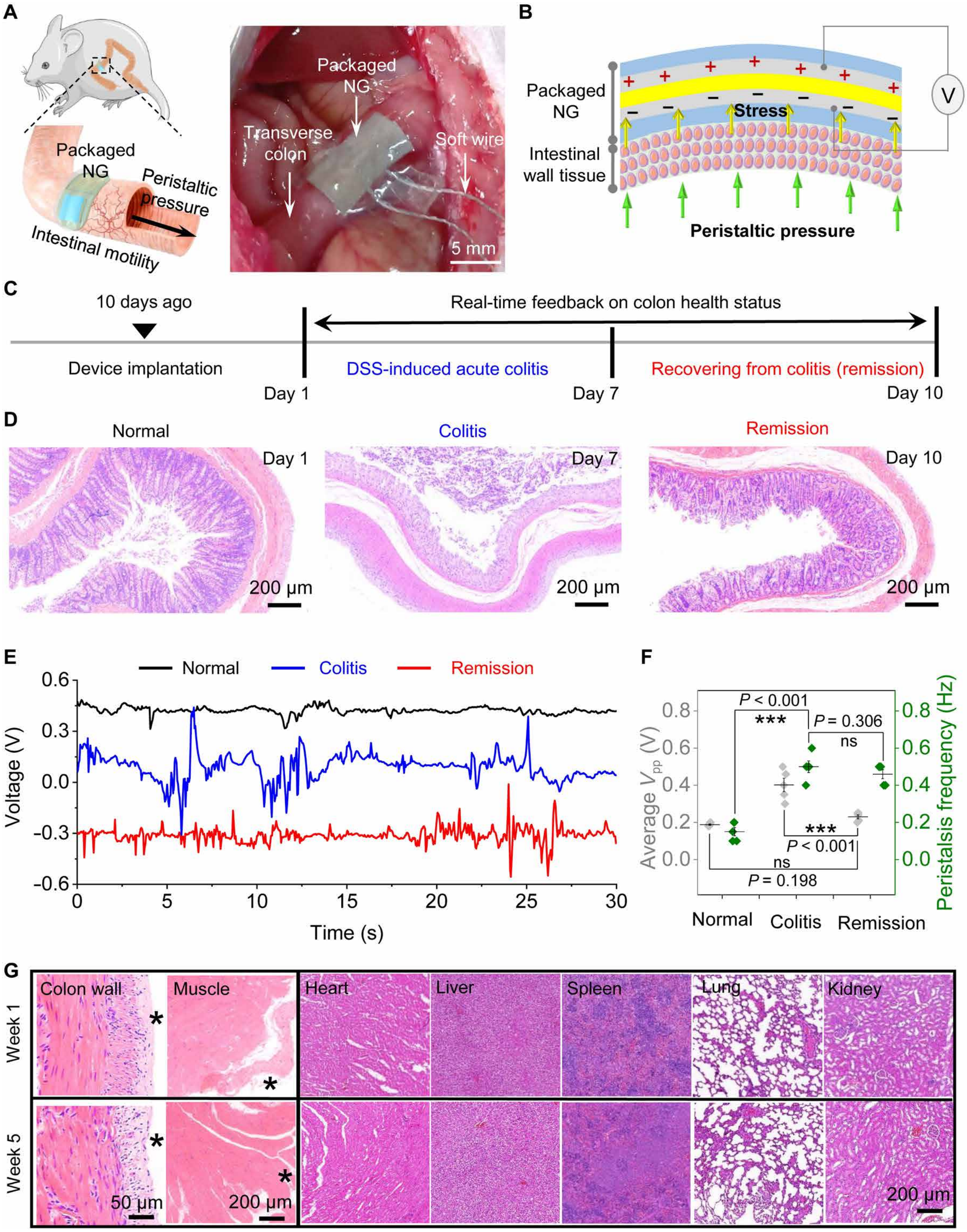

Fig. 4. In vivo applications of core/shell NF-based NG. (**A**) Schematic (left) and surgical image (right) of implantation of the core/shell NF-based NG for recording intestinal peristalsis pressure changes in vivo. Soft wire, soft silver-plated PTFE Teflon wire. (**B**) Schematic illustration of the piezoelectric effect in response to intestinal peristalsis. (**C**) Schematic diagram of the establishment protocols of DSS-induced acute colitis rat model and real-time monitoring by the PLLA/Gly NF-based NGs. (**D**) Representative H&E staining images showing normal (left), colitis (middle), and remission (right) colon tissue from rats. (**E**) Piezoelectric voltage signals induced by colonic motilities when rats were in different physiological states. (**F**) Voltage amplitude (gray) and frequency (green) statistics from the voltage pattern on the left. (**G**) H&E stains of (left) the implanted tissues (colon and skin) and other vital organs (heart, liver, spleen, kidney, and lung) at different time points postimplantation. Asterisks (*) show the implantation location. $n = 5$ biologically independent animals for each group. All error bars indicate ± SD. ***$P < 0.001$; ns, not significant. All P values are evaluated by one-sided analysis of variance (ANOVA) and post-Tukey analysis.

Nonwoven fabrics were fabricated using these core/shell NFs and assembled into ultraflexible NG devices. This device could retain an excellent conformality on heavily wrinkled soft tissue surfaces, such as the colon walls. From ex vivo models and in vivo rat tests, the PLLA/Gly NF NGs could generate an appreciable voltage output following the intestinal movements. This capability may offer in vivo diagnostic functions for the early assessment and prevention of gastrointestinal diseases, such as colitis, intestinal obstruction, Ogilvie's syndrome, and irritable bowel syndrome. It may also serve as a detection platform for preclinical evaluation of previously unidentified gastrointestinal therapeutic drugs. This piezoelectric biomaterial NFs could be extended to other soft organs or tissues, where extremely rough surfaces are commonly interacted. By integrating with wireless data transmission modules, our fabric-based electromechanical sensor patches will achieve wireless, leadless, and passive monitoring and recording of various biomechanical information in vivo for future patient-centered health care systems. This soft piezoelectric material and device design strategy will eventually bring profound impacts to the development of smart biodegradable biomedical electronics in regenerative medicine, drug delivery, and medical therapeutics.

MATERIALS AND METHODS

Fabrication of NFs

PLLA/Gly NFs were fabricated by electrospinning the mixed solution of PLLA (molecular weight of 66,000 to 107,000, Sigma-Aldrich) and Gly (DOT Scientific Inc.) using a #21 nozzle. The electrospinning was conducted using a high DC voltage of 1.5 kV/cm with a solution flow speed at 0.8 ml/hour at room temperature and 35 ± 5% humidity. These fibrous mats were then annealed at 105°C for 10 hours, and then the oven (Yamato Constant Temperature Oven DKN402) was shut off and allowed to cool to room temperature. As-received NFs were stored in vacuum for further experimental operation. For more details of the electrospinning, please see text S1.

Theoretical simulations of the intermolecular interactions between Gly and PLLA

The periodic MD simulation was carried out using the LAMMPS simulation package to explore the RDF of pristine PLLA/Gly composites under an electric field of 1.5 kV/cm. Because Gly, as a nucleating agent, has many hydrogen donors (e.g., nitrogen and oxygen), it enables to form a massive hydrogen bonding network with PLLA chains. For the specific MD modeling process, please refer to text S2. DFT calculation including a long-range dispersion correction, as implemented in the Vienna Ab initio Simulation Package, was used to predict the intermolecular interactions between PLLA and Gly. For more details of the DFT calculation, please see text S3.

Characterizations

Crystallizations of the NFs were characterized by FTIR (Nicolet iS10, Thermo Fisher Scientific), DSC (DSC823e, Mettler Toledo), and 1D and 2D XRD (D8 Advance, Bruker). The morphology and structural distribution were observed by SEM (Supra 55, Carl Zeiss) and TEM (JEM-2100, JEOL). The orientation of the β phase nanocrystals in the NFs was visualized by HRTEM (JEM-2100, JEOL) at an acceleration voltage of 200 kV. The molecular skeleton was analyzed by Raman (inVia, Renishaw). The output voltage was collected by a multimeter (DMM6500, Keithley).

Cytocompatibility in vitro

PC12 cells (CRL-1721, Cell Bank, Shanghai Institutes for Biological Sciences, Chinese Academy of Sciences) were cultured on core/shell NFs and its packaged device or cell plates in six-well plates for 72 hours. The flow cytometer (NovoCyte, Aisen Biological Co. Ltd.) was used to excite cell apoptosis test staining solution at an excitation wavelength of 488 nm to detect cell apoptosis. For cell culture details, see text S7.

Monitoring subtle mechanical deformation changes and long-standing biocompatibility in vivo

Six- to 8-week-old Sprague-Dawley rats (male, 150 to 200 g, Shanghai Bikai Keyi Biotechnology Co. Ltd.) were anesthetized by the intake of isoflurane gas (0.8 to 1.5%) and maintained with 1.0% isoflurane. The shaved abdomen was dissected to expose the rat's colon. The core/shell NF-based devices [size of NFs, 5 mm (width) × 10 mm (length) × 50 μm (thickness)] were attached to the rat's colon in response to its deformation using bioglue. Before implantation, devices were sterilized by ultraviolet light irradiation for 1 hour. Last, the implantation site was rinsed twice with saline and then the muscle and skin were sutured with 4-0 Vicryl sutures. The external wounds are treated with iodophor. Ten days after NG device implantation, colitis was induced by the addition of 3.0% w/v DSS to the drinking water for 7 days. Except for the rats with DSS-induced colitis, all other rats were raised in accordance with the relevant regulations for experimental animals, and they are given regular food and water. For the acute colitis part, the piezoelectric signal was conducted on the seventh day after the rats drank DSS water, while the data collection for the relief colitis part was conducted on the third day after the rats with DSS-induced colitis drank normal water instead of DSS water. The onset and remission of acute colitis were confirmed by H&E staining. The electrical signals generated by the peristalsis-driven PLLA/Gly NF-based NGs of rats in different states (i.e., normal rats, colitis rats, and colitis remission rats) were received by a multimeter (DMM6500, Keithley). To assess its long-term in vivo biocompatibility, the animals were euthanized on days 7 and 35, and tissues were extracted, fixed, sliced, and stained with H&E. The animal experiment protocol was approved by the Nanjing Jinling Hospital (protocol ID: SYXK20220041), and all animals received humane care and were handled in accordance with the Institutional Animal Care and Use Committee approval protocol of the Animal Care Center at the Nanjing Jinling Hospital.

Supplementary Materials

This PDF file includes:

Texts S1 to S7
Figs. S1 to S26
Legend for movie S1

Other Supplementary Material for this manuscript includes the following:

Movie S1

REFERENCES AND NOTES

1. J. C. Anderson, C. Eriksson, Piezoelectric properties of dry and wet bone. *Nature* **227**, 491–492 (1970).
2. W. Li, J. Sigley, M. Pieters, C. C. Helms, C. Nagaswami, J. W. Weisel, M. Guthold, Fibrin fiber stiffness is strongly affected by fiber diameter, but not by fibrinogen glycation. *Biophys. J.* **110**, 1400–1410 (2016).
3. J. Li, Y. Long, F. Yang, X. Wang, Degradable piezoelectric biomaterials for wearable and implantable bioelectronics. *Curr. Opin. Solid State Mater. Sci.* **24**, 100806 (2020).

4. J. Li, Y. Long, F. Yang, H. Wei, Z. Zhang, Y. Wang, J. Wang, C. Li, C. Carlos, Y. Dong, Y. Wu, W. Cai, X. Wang, Multifunctional artificial artery from direct 3D printing with built-in ferroelectricity and tissue-matching modulus for real-time sensing and occlusion monitoring. *Adv. Funct. Mater.* **30**, 2002868 (2020).
5. X. Wang, J. Song, J. Liu, Z. L. Wang, Direct-current nanogenerator driven by ultrasonic waves. *Science* **316**, 102–105 (2007).
6. T. Li, Z. Q. Feng, M. Qu, K. Yan, T. Yuan, B. Gao, T. Wang, W. Dong, J. Zheng, Core/shell piezoelectric nanofibers with spatial self-orientated β-phase nanocrystals for real-time micropressure monitoring of cardiovascular walls. *ACS Nano* **13**, 10062–10073 (2019).
7. T. Li, M. Qu, C. Carlos, L. Gu, F. Jin, T. Yuan, X. Wu, J. Xiao, T. Wang, W. Dong, X. Wang, Z. Q. Feng, High-performance poly(vinylidene difluoride)/dopamine core/shell piezoelectric nanofiber and its application for biomedical sensors. *Adv. Mater.* **33**, e2006093 (2021).
8. G. Yao, L. Kang, C. Li, S. Chen, Q. Wang, J. Yang, Y. Long, J. Li, K. Zhao, W. Xu, W. Cai, Y. Lin, X. Wang, A self-powered implantable and bioresorbable electrostimulation device for biofeedback bone fracture healing. *Proc. Natl. Acad. Sci. U.S.A.* **118**, e2100772118 (2021).
9. L. Gu, J. Liu, N. Cui, Q. Xu, T. Du, L. Zhang, Z. Wang, C. Long, Y. Qin, Enhancing the current density of a piezoelectric nanogenerator using a three-dimensional intercalation electrode. *Nat. Commun.* **11**, 1030 (2020).
10. H. S. Lee, J. Chung, G. T. Hwang, C. K. Jeong, Y. Jung, J. H. Kwak, H. Kang, M. Byun, W. D. Kim, S. Hur, A.-H. Oh, K. J. Lee, Flexible inorganic piezoelectric acoustic nanosensors for biomimetic artificial hair cells. *Adv. Funct. Mater.* **24**, 6914–6921 (2014).
11. F. Yang, J. Li, Y. Long, Z. Zhang, L. Wang, J. Sui, Y. Dong, Y. Wang, R. Taylor, D. Ni, W. Cai, P. Wang, T. Hacker, X. Wang, Wafer-scale heterostructured piezoelectric bio-organic thin films. *Science* **373**, 337–342 (2021).
12. E. J. Curry, T. T. Le, R. Das, K. Ke, E. M. Santorella, D. Paul, T. M. Chorsi, K. T. M. Tran, J. Baroody, E. R. Borges, B. Ko, A. Golabchi, X. Xin, D. Rowe, L. Yue, J. Feng, M. D. Morales-Acosta, Q. Wu, I.-P. Chen, X. T. Cui, J. Pachter, T. D. Nguyen, Biodegradable nanofiber-based piezoelectric transducer. *Proc. Natl. Acad. Sci. U.S.A.* **117**, 214–220 (2020).
13. Y. Shao, S. Yan, J. Li, Z. Silva-Pedraza, T. Zhou, M. Hsieh, B. Liu, T. Li, L. Gu, Y. Zhao, Y. Dong, B. Yin, X. Wang, Stretchable encapsulation materials with high dynamic water resistivity and tissue-matching elasticity. *ACS Appl. Mater. Interfaces* **14**, 18935–18943 (2022).
14. R. Yang, Y. Qin, C. Li, G. Zhu, Z. L. Wang, Converting biomechanical energy into electricity by a muscle-movement-driven nanogenerator. *Nano Lett.* **9**, 1201–1205 (2009).
15. M. Yang, J. Liu, D. Liu, J. Jiao, N. Cui, S. Liu, Q. Xu, Y. Qin, A fully self-healing piezoelectric nanogenerator for self-powered pressure sensing electronic skin. *Research* **2021**, 9793458 (2021).
16. J. Li, L. Kang, Y. Yu, Y. Long, J. J. Jeffery, W. Cai, X. Wang, Study of long-term biocompatibility and bio-safety of implantable nanogenerators. *Nano Energy* **51**, 728–735 (2018).
17. Y. Yu, H. Sun, H. Orbay, F. Chen, C. G. England, W. Cai, X. Wang, Biocompatibility and in vivo operation of implantable mesoporous PVDF-based nanogenerators. *Nano Energy* **27**, 275–281 (2016).
18. D. Da Silva, M. Kaduri, M. Poley, O. Adir, N. Krinsky, J. Shainsky-Roitman, A. Schroeder, Biocompatibility, biodegradation and excretion of polylactic acid (PLA) in medical implants and theranostic systems. *Chem. Eng. J.* **340**, 9–14 (2018).
19. S. Lee, M. K. Joshi, A. P. Tiwari, B. Maharjan, K. S. Kim, Y. H. Yun, C. H. Park, C. S. Kim, Lactic acid assisted fabrication of bioactive three-dimensional PLLA/β-TCP fibrous scaffold for biomedical application. *Chem. Eng. J.* **347**, 771–781 (2018).
20. S. Farah, D. G. Anderson, R. Langer, Physical and mechanical properties of PLA, and their functions in widespread applications—A comprehensive review. *Adv. Drug Deliv. Rev.* **107**, 367–392 (2016).
21. Y. Tajitsu, Fundamental study on improvement of piezoelectricity of poly(ʟ-lactic acid) and its application to film actuators. *IEEE Trans. Ultrason. Ferroelectr. Freq. Control* **60**, 1625–1629 (2013).
22. M. Ando, H. Kawamura, H. Kitada, Y. Sekimoto, T. Inoue, Y. Tajitsu, Pressure-sensitive touch panel based on piezoelectric poly(L-lactic acid) film. *Jpn. J. Appl. Phys.* **52**, 09KD17 (2013).
23. M. Ando, H. Kawamura, H. Kitada, Y. Sekimoto, T. Inoue, Y. Tajitsu, New human machine interface devices using a piezoelectric poly(L-lactic acid) film, in *2013 Joint IEEE International Symposium on Applications of Ferroelectric and Workshop on Piezoresponse Force Microscopy (ISAF/PFM)* (IEEE, 2013), pp. 236–239.
24. E. J. Curry, K. Ke, M. T. Chorsi, K. S. Wrobel, A. N. Miller III, A. Patel, I. Kim, J. Feng, L. Yue, Q. Wu, C. L. Kuo, K. W. Lo, C. T. Laurencin, H. Ilies, P. K. Purohit, T. D. Nguyen, Biodegradable piezoelectric force sensor. *Proc. Natl. Acad. Sci. U.S.A.* **115**, 909–914 (2018).
25. M. Smyth, V. Poursorkhabi, A. K. Mohanty, S. Gregori, M. Misra, Electrospinning highly oriented and crystalline poly(lactic acid) fiber mats. *J. Mater. Sci.* **49**, 2430–2441 (2014).
26. A. R. Cho, D. M. Shin, H. W. Jung, J. C. Hyun, J. S. Lee, D. Cho, Y. L. Joo, Effect of annealing on the crystallization and properties of electrospun polylatic acid and nylon 6 fibers. *J. Appl. Polym. Sci.* **120**, 752–758 (2011).
27. V. Sencadas, C. Ribeiro, A. Heredia, I. K. Bdikin, A. L. Kholkin, S. Lanceros-Méndez, Local piezoelectric activity of single poly(L-lactic acid) (PLLA) microfibers. *Appl. Phys. A* **109**, 51–55 (2012).
28. R. Pantani, A. Sorrentino, Influence of crystallinity on the biodegradation rate of injection-moulded poly(lactic acid) samples in controlled composting conditions. *Polym. Degrad. Stab.* **98**, 1089–1096 (2013).
29. G. Bassotti, G. de Roberto, F. Chistolini, F. Sietchiping-Nzepa, O. Morelli, A. Morelli, Twenty-four-hour manometric study of colonic propulsive activity in patients with diarrhea due to inflammatory (ulcerative colitis) and non-inflammatory (irritable bowel syndrome) conditions. *Int. J. Colorectal Dis.* **19**, 493–497 (2004).

Acknowledgments

Funding: This work was partially supported by the National Heart, Lung, and Blood Institute of the National Institutes of Health under award number R01HL157077 for materials developments and the National Institute of Biomedical Imaging and Bioengineering of the National Institutes of Health under award number R01EB034241 for device developments. The content is solely the responsibility of the authors and does not necessarily represent the official views of the National Institutes of Health. Z.W. thanks the Science and Technology Planning Project of Guangdong Province (2021A0505110002). **Author contributions:** Conceptualization: T.L., Y.Y., S.Y., Y.D., S.W., Z.W., and X.W. Methodology: T.L., J.L., Y.Y., S.Y., W.W., and X.W. Investigation: T.L., L.G., Y.Y., Y.S., S.Y., Y.Z., X.W., H.Q., C.C., and S.W. Visualization: T.L., L.G., Y.Y., W.W., Y.S., S.Y., C.C., and S.W. Software: S.Y., Y.Y., and S.W. Formal analysis: T.L., Y.Y., S.Y., and S.W. Resources: T.L., Y.Y., Y.S., S.Y., Y.Z., H.Q., S.W., and X.W. Data curation: Y.Y., S.Y., S.W., and X.W. Validation: T.L., Y.Y., Y.S., S.Y., Y.Z., S.W., and Z.W. Funding acquisition: Y.Y., S.W., Z.W., and X.W. Project administration: T.L., S.Y., Y.Y., S.W., and X.W. Supervision: Y.Y., S.Y., S.W., and X.W. Writing—original draft: T.L., L.G., Y.Y., S.Y., W.W., and S.W. Writing—review and editing: T.L., L.G., Y.Y., S.Y., X.W., W.W., S.W., and X.W. **Competing interests:** The authors declare that they have no competing interests. **Data and materials availability:** All data needed to evaluate the conclusions in the paper are present in the paper and/or the Supplementary Materials.

Submitted 4 January 2024
Accepted 14 June 2024
Published 19 July 2024
10.1126/sciadv.adn8706